

# Contents

<b>4</b>	<b>Analysis and modelling of subgrid tendencies</b>	<b>1</b>
4.1	Calculation of subgrid tendencies . . . . .	1
4.2	Choice of coarse-graining method . . . . .	2
4.3	Analysis of subgrid tendencies . . . . .	4
4.4	Modelling of subgrid tendencies . . . . .	9

*This page intentionally left blank*

## Chapter 4

# Analysis and modelling of subgrid tendencies

In [Chapter 3](#) I investigated the resolution dependence of several metrics in order to choose the resolutions of the fine “truth” model and the coarse “control” model needed for data-driven parametrisation. [Table 4.1](#) shows the final choices; for the remainder of this thesis, the terms “fine model” and “coarse model” will refer to the settings shown in the Table.

	Fine model	Coarse model
$N_x$	2048	256
$N_z$	256	64
$\Delta t$	$1.0 \times 10^{-3}$	$5.333 \times 10^{-3}$

Table 4.1: Resolutions  $(N_x, N_z)$  and time steps  $\Delta t$  chosen for the fine and coarse models.

The aim of this chapter is to construct a data-driven parametrisation scheme for the Rayleigh-Bénard problem. [§ 4.1](#) will establish the method used to calculate subgrid tendencies and generate the training dataset. [§ 4.2](#) will identify and resolve some subtle issues associated with the coarse-graining step of the method. In [§ 4.3](#), I will perform exploratory analysis of the training dataset to identify correlations that could be used as the bases of data-driven parametrisation schemes, before constructing and fitting the final scheme in [§ 4.4](#).

### 4.1 Calculation of subgrid tendencies

Following the generic method of Brajard et al. (2021), which was reviewed in [§ 1.3.2](#), it is possible to define subgrid tendencies for the Rayleigh-Bénard problem and implement a workflow for calculating them using high- and low-resolution numerical models. This workflow is described below and illustrated as a flowchart in [Figure 4.1](#), which uses the same numbering to show the order of the steps.

1. The fine model was integrated for 300 time units, the initial condition being the end of the  $2048 \times 256$  simulation in [Chapter 3](#). Every 3 time units, the model state was saved, and then saved again one time step later. This resulted in a dataset of 100 pairs of snapshots separated by 3 time units. An interval of 3 time units was chosen as it was the approximate decorrelation time of the model variables (see [Appendix B.3](#)); using a shorter interval would result in saving redundant information.
2. Each pair of snapshots was *coarse-grained*, reducing its spatial resolution to that of the coarse model. The nature of the coarse-graining operation warrants special attention and is discussed

separately in § 4.2.

3. The first coarse-grained snapshot in each pair was input as an initial condition for the coarse model. The coarse model integrated for one time step only, and the resulting state—the coarse model’s prediction for the large-scale state after one time step—was saved.
4. The first coarse-grained snapshot in each pair from Step 2 was subtracted from the second and the difference divided by the fine model’s time step, giving the *true coarse tendency* (i.e., the true time derivative of the large-scale state as calculated by the fine model).
5. The first coarse-grained snapshot in each pair from Step 2 was subtracted from the coarse model prediction produced in Step 3 and the difference divided by the coarse model’s time step, giving the tendency predicted by the coarse model (i.e., its prediction of the time derivative of the large-scale state).
6. Finally, the coarse model predicted tendencies from Step 5 were subtracted from the true coarse tendencies from Step 4, producing the *subgrid tendencies*. These measure the error (or, more precisely, minus the error) in the coarse model’s prediction of the time derivative of the large-scale state, and would be identically zero for a perfect coarse model.

The goal will be to approximate the subgrid tendencies (labelled “predictand” in Figure 4.1) as functions of the coarse state (labelled “predictor”). In Chapter 5, I construct a new coarse model that adds the approximate subgrid tendencies to the original predicted tendencies, thereby obtaining a better approximation to the true coarse tendency. When integrated, the new coarse model should, in principle, yield a solution that more closely matches the coarse-grained solution of the fine model.

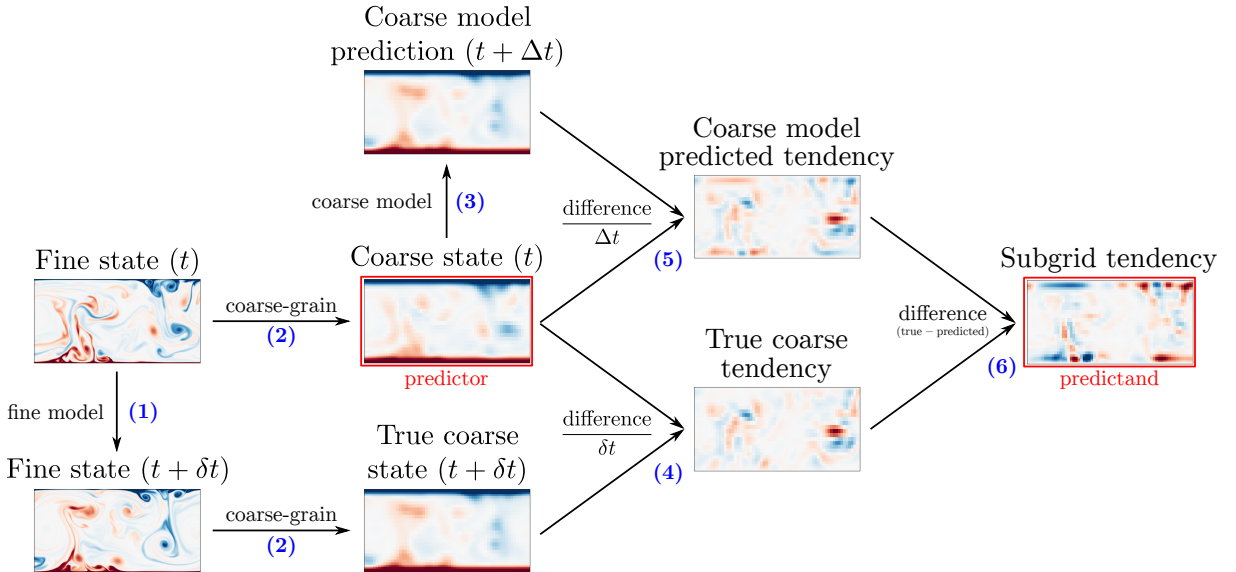


Figure 4.1: Flowchart illustrating the procedure used to calculate subgrid tendencies. The plots show an example of the workflow being applied to the temperature data but are for illustrative purposes only. The blue numbers correspond to the steps described in the text.

## 4.2 Choice of coarse-graining method

Coarse-graining is the process of reducing a gridded dataset onto a lower-resolution grid, and it is required at Step 2 of the workflow described in § 4.1. It was found that the choice of coarse-graining method was

a major influence on the quality of the calculated subgrid tendencies; this is the consequence of a subtle issue that may seem purely semantic at first but in fact has important practical implications.

In general, the output of a coarse (i.e., reduced-order) model is meant to approximate a certain *representation* of the output of a chosen fine model. To give three concrete examples, the coarse model might seek to reproduce (a) the values of the high-resolution fields on a sparser grid of points, or (b) the averages over a set of larger grid boxes, or (c) the first  $N$  coefficients of the discrete Fourier transform (where  $N$  is less than the number of coefficients needed to fully determine the original fields). The modeller has the freedom choose a representation, which in turn determines how the output of the coarse model should be interpreted. The choice of representation also implicitly determines a coarse-graining operation: a map from the state space of the fine model to the state space of the coarse model that isolates the necessary large-scale information and discards the rest. Referring to the previous examples, option (a) calls for an operation that simply discards, say, three out of every four or nine out of ten grid points. Option (b) calls for the grouping and averaging of the grid points that lie within each large grid box. Option (c) calls for the truncation of fine fields at the  $N$ th coefficient in Fourier space.

The key lesson that was learnt during the course of this work is that the chosen representation and coarse-graining method must be appropriate to the nature of the coarse model. In this work, the coarse model was a Dedalus solver that, in [Step 3](#) of the workflow in [§ 4.1](#), received gridded initial condition data in real space and integrated the governing equations forward in time using the same numerical method as the fine model. This gave rise to two constraints on the coarse-graining method:

1. The coarse-grained initial condition must be well-resolved on the coarse model's grid. Numerical solution algorithms for PDEs assume (e.g., by approximating derivatives as finite differences) that the solution is well-resolved on the discrete model grid, and can become unstable or produce output marred by artefacts if this condition is not met.
2. The initial condition must respect physical constraints, namely the divergence-free condition [\(3.9\)](#) and the boundary conditions [\(3.10\)–\(3.12\)](#). A numerical algorithm cannot be expected to behave predictably when presented with unphysical initial conditions.

During the development of this study, before the above requirements were known, coarse-graining was performed by averaging the fine grid points that lay within each coarse grid box (a method known within the Earth sciences as *first-order conservative remapping* or *regridding* because it preserves mean values; see [Jones 1999](#)). [Figure 4.2](#), illustrating the application of first-order conservative regridding to sample temperature data, demonstrates that the result is not very well-resolved on the coarse grid; in many places, adjacent grid points have sharp differences in temperature. First-order conservative regridding is also not guaranteed to preserve boundary values or the divergence-free nature of the velocity field. Consequently, the tendencies obtained from the coarse model in [Step 5](#) of the workflow suffered from noise and numerical artefacts that propagated to the subgrid tendencies in [Step 6](#). With the signal of interest obscured, it was impossible to model the subgrid tendencies as functions of the coarse state.

It was evident that the coarse-graining method needed to involve a smoothing operation of some kind. However, most conventional smoothing methods, such as Gaussian filtering, also fail to preserve the boundary and divergence-free conditions. The solution to this problem was to supply each snapshot of the fine model state as an initial condition to an appropriate system of PDEs, chosen so that the integration of the system would have a smoothing effect on the initial condition data. The key advantage of this approach is that the boundary and divergence-free conditions can be explicitly enforced.

The choice of PDEs to achieve this was inspired by classical Gaussian filtering. Recall that a Gaussian filter convolves input data with a filter kernel that takes the form of a Gaussian function, which also happens to be the Green's function for the heat equation  $\partial\psi/\partial t = \nabla^2\psi$  in an *infinite* domain. It follows that heat equations of some form on the *finite* domain of the Rayleigh-Bénard problem (whose Green's functions are not Gaussian) will have a similar smoothing effect while preserving the required boundary conditions. The appropriate equation for smoothing the temperature field  $\theta$  is therefore

$$\frac{\partial\theta}{\partial t} = \nabla^2\theta \tag{4.1}$$

on  $[0, \Gamma] \times [0, 1]$  with  $\theta(z = 0) = +1/2$ ,  $\theta(z = 1) = -1/2$  and  $\theta(x = 0) = \theta(x = \Gamma)$ . It is tempting to propose an equation of the same form,  $\partial \mathbf{u} / \partial t = \nabla^2 \mathbf{u}$ , for the velocity field, but its solution on the finite domain would not necessarily preserve  $\nabla \cdot \mathbf{u} = 0$ . By analogy to the incompressible Navier-Stokes equations, it is necessary to introduce a “pressure” term  $-\nabla \pi$  on the right-hand side, with the additional field  $\pi(x, z)$  giving an additional degree of freedom that allows one to impose  $\nabla \cdot \mathbf{u} = 0$  without over-determining the problem. The velocity field is thus smoothed by the equations

$$\frac{\partial \mathbf{u}}{\partial t} = -\nabla \pi + \nabla^2 \mathbf{u} \quad \text{and} \quad (4.2)$$

$$\nabla \cdot \mathbf{u} = 0 \quad (4.3)$$

on  $[0, \Gamma] \times [0, 1]$  with  $\mathbf{u}(z = 0) = \mathbf{u}(z = 1) = \mathbf{0}$  and  $\mathbf{u}(x = 0) = \mathbf{u}(x = \Gamma)$ . The equations (4.1)–(4.3) were integrated numerically on the same grid as the fine model using a solver that was straightforwardly implemented in Dedalus.

Once the high-resolution data had been smoothed using the method described above, all that remained was to downsample the result to the resolution of the coarse model. Downsampling was handled by Dedalus via truncation in spectral coefficient space. To summarise, the coarse-graining workflow is as follows:

1. Input a high-resolution snapshot as the initial condition for the solver of (4.1)–(4.3).
2. Integrate the solver for  $10^{-3}$  time units (the duration that was found to produce the necessary amount of smoothing) in steps of  $2 \times 10^{-4}$  time units.
3. Downsample the final state to the resolution of the coarse model and save the result.
4. Reset the solver and return to [Step 1](#) to coarse-grain the next high-resolution snapshot.

[Figure 4.2](#) compares the results of the improved coarse-graining method and first-order conservative regridding for the temperature field. Close inspection of the figure shows that the improved coarse-graining method produces smooth results that are well-resolved on the coarse grid, in contrast to first-order conservative regridding.

## 4.3 Analysis of subgrid tendencies

In this section, I will analyse the subgrid tendency data by plotting joint histograms of subgrid tendencies (the predictands) against coarse state variables and other quantities derived from the coarse state variables (the predictors). At each time step, predictor and predictand fields were sampled using linear interpolation at  $256 \times 64 = 16384$  random, uniformly distributed points in the domain<sup>1</sup>.

The obvious first step is to plot joint histograms for the subgrid tendencies of  $u$ ,  $w$  and  $\theta$  against the values of  $u$ ,  $w$  and  $\theta$  themselves. [Figure 4.3](#) shows all  $3 \times 3 = 9$  possible histograms, as well as the marginal distributions. There are no immediately obvious correlations; each joint distribution appears similar to the product of its corresponding marginal distributions. This finding contrasts with the well-known results for the Lorenz ’96 model that were discussed in [Chapter 2](#). While [Figure 2.2](#) showed that the subgrid tendencies of Lorenz ’96 can, to a large extent, be predicted directly from the values of the resolved variables, the problem is evidently more complex for Rayleigh-Bénard convection.

Take note, however, of the unusual shape of the joint distribution of the  $\theta$  subgrid tendency against  $w$  (bottom row, second from left in [Figure 4.3](#)). It does not appear to be a simple product of the marginal distributions, instead having a slanted linear feature near  $w = 0$ . The origin of this feature is revealed by conditioning on the vertical coordinate  $z$  (or, in other words, using  $z$  as a second predictor

<sup>1</sup>It is necessary to randomly sample the fields in this way, rather than using the raw gridded data, to remove artefacts that appear in the histograms when large groups of sampling points share the exact same vertical position  $z$ .

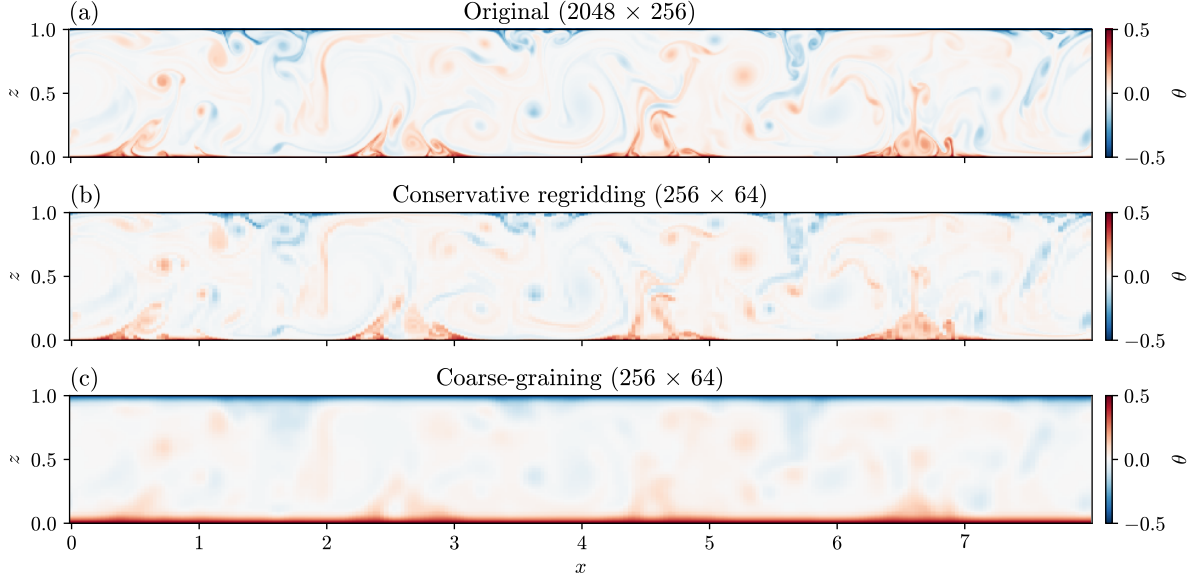


Figure 4.2: **(a)** A snapshot of the temperature field in a simulation with  $2048 \times 256$  resolution; **(b)** the field in (a) after first-order conservative regridding to  $256 \times 64$  (poorly resolved on the coarse grid); **(c)** the field in (a) after coarse-graining to  $256 \times 64$  using the method in the text (smooth and well-resolved on the coarse grid).

in addition to  $w$ ). I achieve this by plotting, in Figure 4.4, a series of joint histograms, each one using samples from a different horizontal slice of the domain. When sampling is restricted to  $z \in [0.0, 0.1]$  or  $z \in [0.9, 1.0]$ , a negative correlation is revealed. This means that the coarse model tends to overestimate the rate of temperature change when the vertical velocity is positive (requiring a negative subgrid tendency correction) and underestimate it when the vertical velocity is negative (requiring a positive correction). This correlation is not present in the middle of the domain, indicating that the slanted feature in the original histogram originates in the boundary layers.

Another option is to use the derivatives of  $u$ ,  $w$  and  $\theta$  (computed using finite differences) as predictors. Figures 4.5–4.7 show similar conditional joint histograms for three of the possible pairings, namely  $\theta$  subgrid tendency against  $\partial u/\partial x$ ,  $u$  subgrid tendency against  $\partial u/\partial z$  and  $w$  subgrid tendency against  $\partial u/\partial x$ . These also reveal correlations that only exist near the top and bottom of the domain; interestingly, there is a markedly nonlinear correlation for the last pair. Overall, it is unsurprising that the subgrid tendency statistics are position-dependent, since the system lacks a vertical translation symmetry. This is another point of contrast with the Lorenz '96 system (see Chapter 2).

Another observation from Figures 4.4–4.6 is that the subgrid tendencies of  $u$  and  $\theta$  both have noticeably larger variances near the top and bottom of the domain than in the middle. In other words, the coarse model tends to suffer from larger errors in the near-wall regions, suggesting that parametrisation may play a more important role in these places. This is reminiscent of the findings of Stevens, Verzicco, and Lohse (2010), who (as discussed in § 3.5.2) reported insufficient thermal dissipation near the side walls in under-resolved simulations of Rayleigh-Bénard convection in a cylindrical cavity. It is also reminiscent of recent work by Alieva et al. (2023), who, in developing machine-learning-augmented Rayleigh-Bénard simulations, found that short-term forecast and long-term statistical accuracy were optimised when the ML correction was only applied in the near-wall regions.



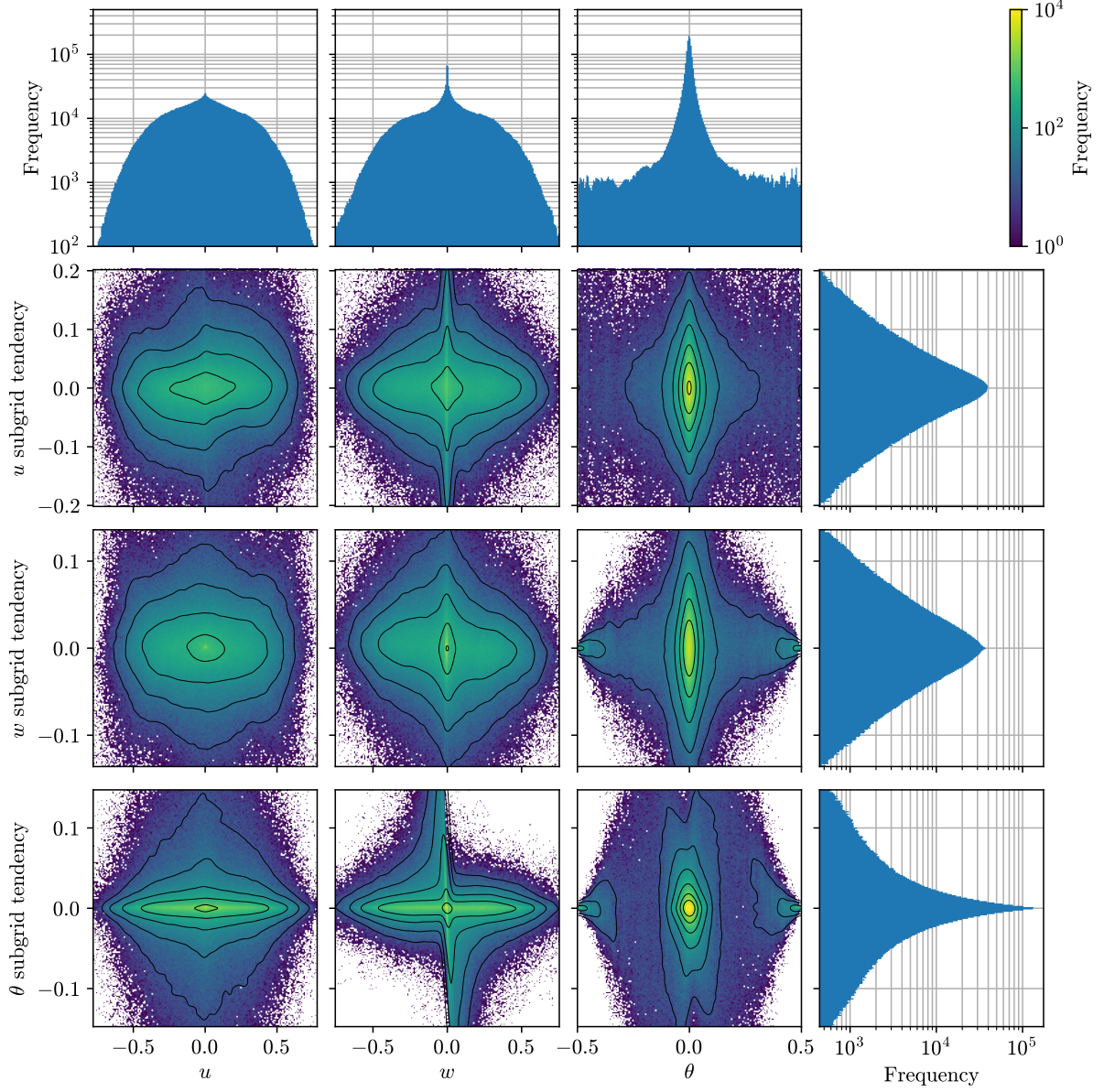


Figure 4.3: Joint histograms of the  $u$ ,  $w$  and  $\theta$  subgrid tendencies against the values of  $u$ ,  $w$  and  $\theta$  themselves (main 3-by-3 grid of pseudocolour plots); and marginal distributions (top row and right column). Note that the joint histograms use a logarithmic colour scale; smoothed contours (black) are plotted at constant intervals in log-space.



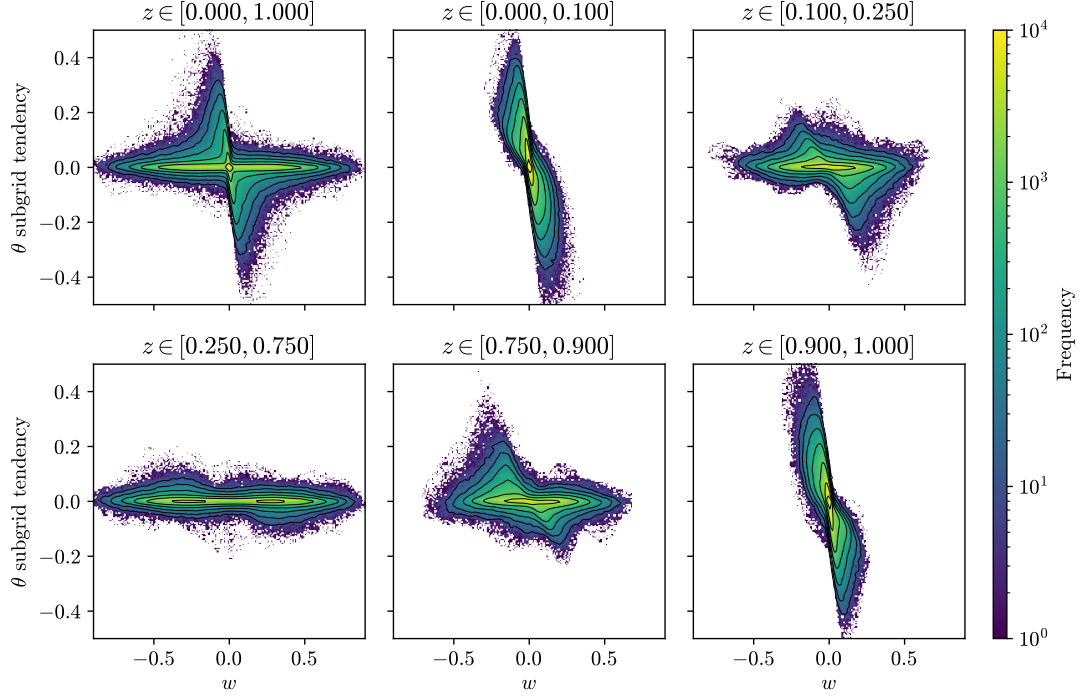


Figure 4.4: Joint histograms of the  $\theta$  subgrid tendency against  $w$ , conditioned on  $z$ . The top left panel shows the unconditioned histogram from Figure 4.3; the others only use samples from certain horizontal slices of the domain, as indicated by their titles.

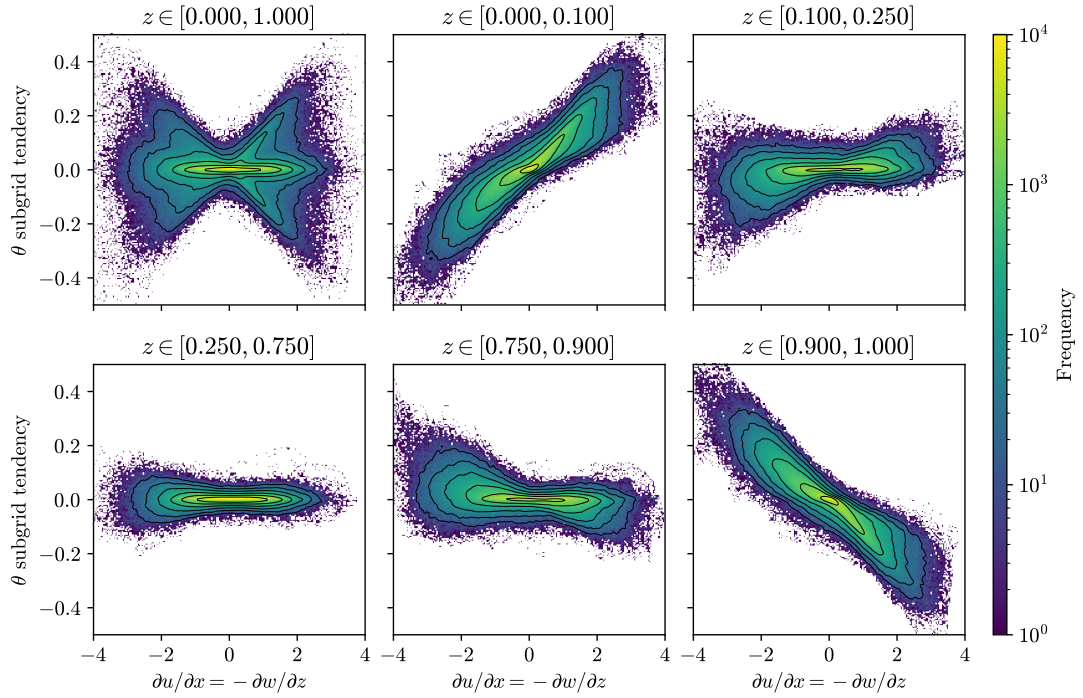


Figure 4.5: The equivalent of Figure 4.4 for the  $\theta$  subgrid tendency against  $\partial u/\partial x$  (which is equal to  $-\partial w/\partial z$  due to incompressibility).

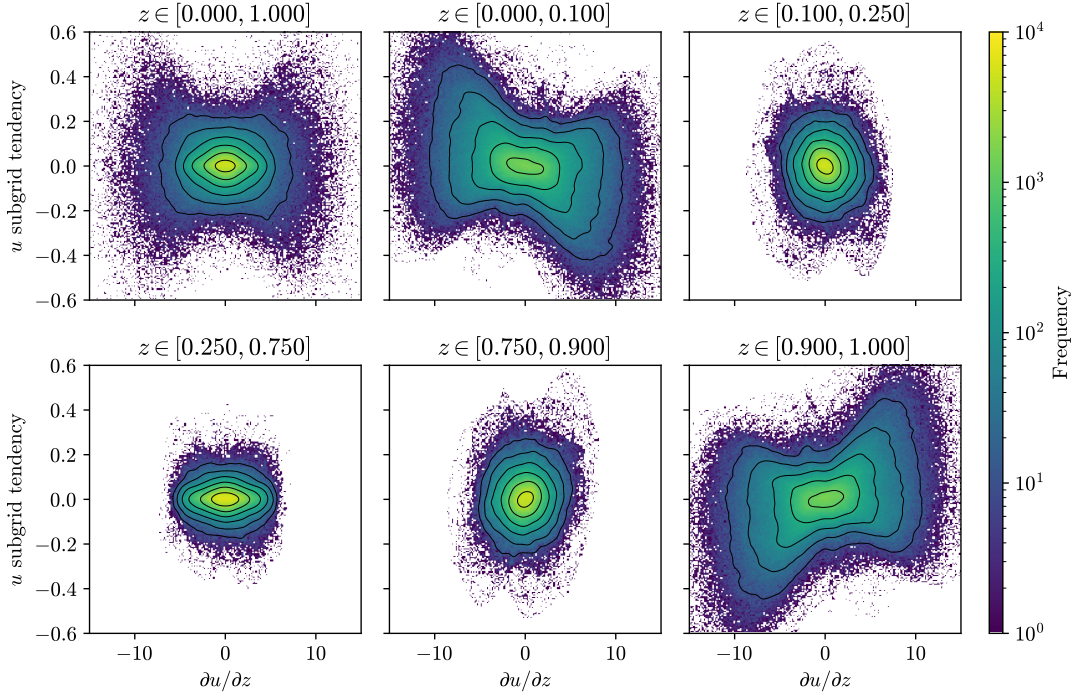


Figure 4.6: The equivalent of Figure 4.4 for the  $u$  subgrid tendency against  $\partial u / \partial z$ .

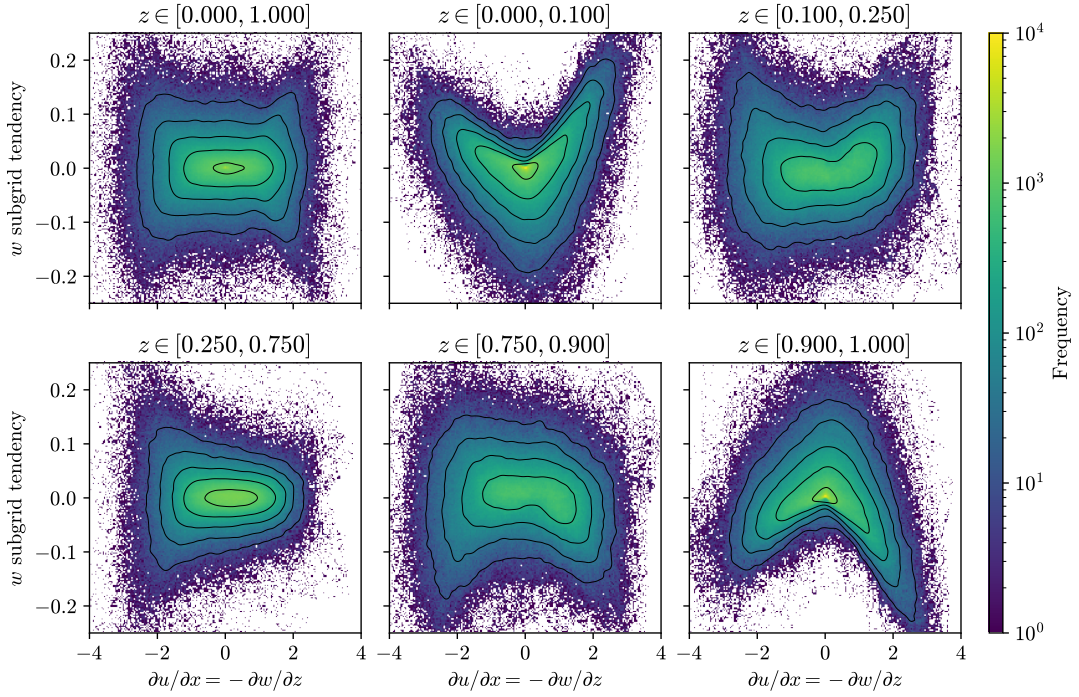


Figure 4.7: The equivalent of Figure 4.4 for the  $w$  subgrid tendency against  $\partial u / \partial x$  (which is equal to  $-\partial w / \partial z$  due to incompressibility).

Yet another possibility is to use the coarse model's predicted *tendencies* (calculated in Step 5 of § 4.1) as predictors for the subgrid tendencies. After all, the tendencies are functions—given by the governing equations (3.13)–(3.15)—of  $u$ ,  $w$ ,  $\theta$  and their derivatives. I again generate joint histograms, conditioned on  $z$ , for each variable's subgrid tendency against its predicted tendency; these are shown in Figures 4.8–4.10. For all three variables, a negative linear correlation appears in the near-wall regions; furthermore, the distributions in these regions appear to lie roughly along a line with slope  $-1$ . This is an interesting and unexpected result because it indicates that the magnitudes of the coarse model's predicted tendencies systematically exceed the magnitudes of the true tendencies, calling for subgrid corrections that almost completely cancel the predictions. Interestingly, there appears to be a slight *positive* correlation in the middle of the domain for  $u$  (Figure 4.9d) and  $w$  (Figure 4.10d), indicating that the coarse model is underestimating the magnitudes of the tendencies in this region.

To summarise, there is evidence of:

1. A negative correlation between  $\theta$  subgrid tendency and  $w$  near  $z = 0, 1$ ,
2. A positive correlation between  $\theta$  subgrid tendency and  $\partial u / \partial x$  near  $z = 0$  and a negative correlation near  $z = 1$ ,
3. A weak negative correlation between  $u$  subgrid tendency and  $\partial u / \partial z$  near  $z = 0$  and a weak positive correlation near  $z = 1$ ,
4. A nonlinear correlation between  $w$  subgrid tendency and  $\partial u / \partial x$  near  $z = 0, 1$ , and
5. A negative correlation between each variable's subgrid tendency and the corresponding tendency predicted by the coarse model, near  $z = 0, 1$ .

In § 6.3 I will propose a physical explanation that links Items 1 and 2 and the  $\theta$  part of Item 5, conjecturing that similar explanations exist for the others.

## 4.4 Modelling of subgrid tendencies

There are several correlations that could be exploited to construct a parametrisation scheme for modelling the subgrid tendencies as functions of the coarse state variables. I choose to use the relationship between subgrid tendencies and predicted tendencies, as it admits a particularly simple parametrisation.

Observing that the subgrid tendencies (which I now denote by  $\mathcal{S}_\chi$ , where  $\chi = u, w, \theta$ ) are linearly correlated with the predicted tendencies (denoted by  $\mathcal{P}_\chi$ ) for any given  $z$ , I propose a statistical model of the form

$$\mathcal{S}_\chi = f_\chi(z) \mathcal{P}_\chi. \quad (4.4)$$

The function  $f_\chi(z)$  determines the slope of the linear relationship at height  $z$ . (4.4) is an attractive choice because it can be easily coupled into the coarse model as a parametrisation scheme. To the right-hand side of the unparametrised coarse model equations  $\partial \chi / \partial t = \mathcal{P}_\chi$ , one simply adds the model for the subgrid tendencies, meaning that the equations for the parametrised model are simply

$$\frac{\partial \chi}{\partial t} = \mathcal{P}_\chi + \mathcal{S}_\chi = [1 + f_\chi(z)] \mathcal{P}_\chi. \quad (4.5)$$

It remains to determine  $f_\chi(z)$ . The conditional distributions in Figures 4.8–4.10 seem to be symmetric about  $z = 1/2$  (i.e., the histograms for  $z \in [0, 0.05]$  and  $z \in [0.1, 0.15]$  look very similar to those for  $z \in [0.95, 1]$  and  $z \in [0.85, 0.9]$  respectively), so I assume that  $f_\chi(z)$  is a polynomial containing only even powers of  $(z - 1/2)$ . The statistical model (4.4) can then be expanded out as

$$\mathcal{S}_\chi = \beta_0 \mathcal{P}_\chi + \beta_1 (z - 1/2)^2 \mathcal{P}_\chi + \beta_2 (z - 1/2)^4 \mathcal{P}_\chi + \cdots + \beta_N (z - 1/2)^{2N} \mathcal{P}_\chi, \quad (4.6)$$

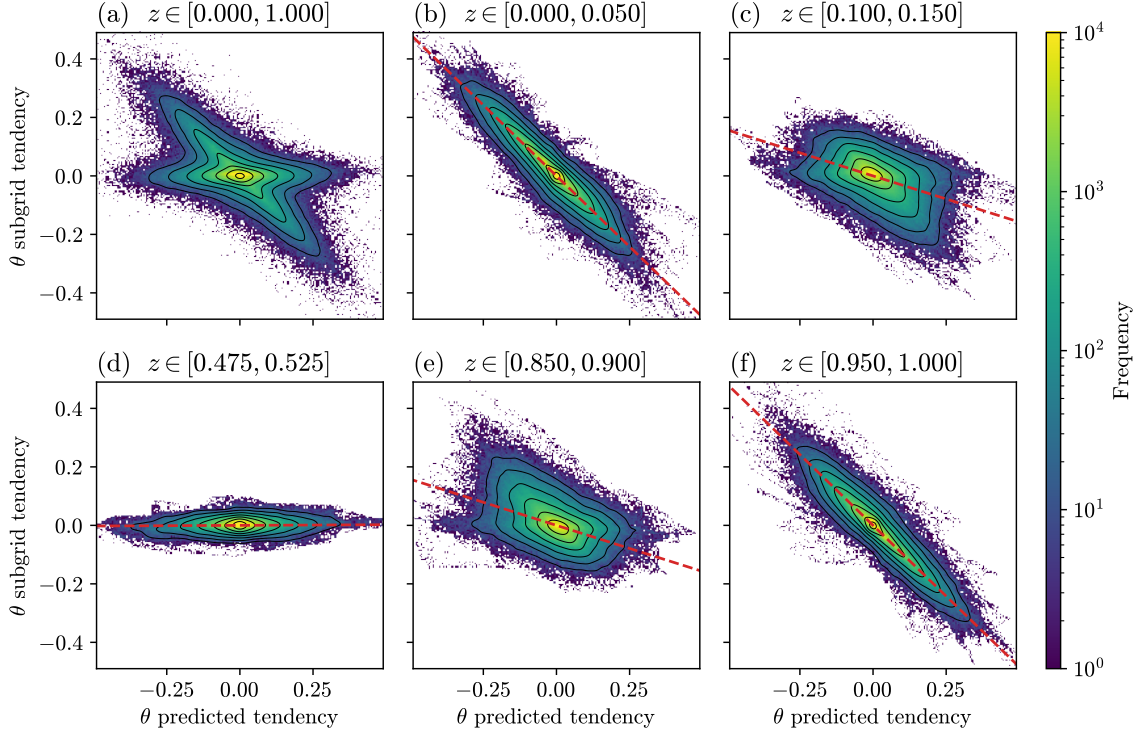


Figure 4.8: The equivalent of Figure 4.4 for the  $\theta$  subgrid tendency against the  $\theta$  tendency predicted by the coarse model.

where  $\beta_i$  are free parameters and  $N$  determines the degree of the polynomial. Because the model is linear in the  $\beta_i$ , it can be efficiently fitted to the training data using ordinary least squares (OLS).

OLS fitting was performed using the `statsmodels` package in Python. A choice of  $N = 10$  for (4.6) was found to produce the best fit. On top of each conditional histogram in Figures 4.8–4.10 I have plotted the line  $\mathcal{S}_\chi = f_\chi(z) \mathcal{P}_\chi$ , where  $f_\chi$  is evaluated at the middle of the  $z$  interval used for conditioning. Table 4.2 shows the coefficients of determination  $R^2$  for each variable. With  $R^2 = 0.769$ , the subgrid tendency of  $\theta$  is captured fairly well. On the other hand, while Figures 4.9 and 4.10 show that the fits for  $u$  and  $w$  have the expected form (slope  $f_\chi(z)$  close to -1 for  $z$  near 0 and 1, and close to 0 elsewhere), their low coefficients of determination indicate that the residuals are substantial and the use of (4.6) is unlikely to add much value (especially for  $w$ ).

Variable	$R^2$
$\theta$	0.769
$u$	0.357
$w$	0.079

Table 4.2: Coefficients of determination  $R^2$  for the OLS regression of each variable’s subgrid tendency against its predicted tendency according to (4.6).

Thus concludes the analysis and modelling of the subgrid tendencies; Chapter 5 will take the next step of coupling the fitted parametrisation scheme into the coarse model.



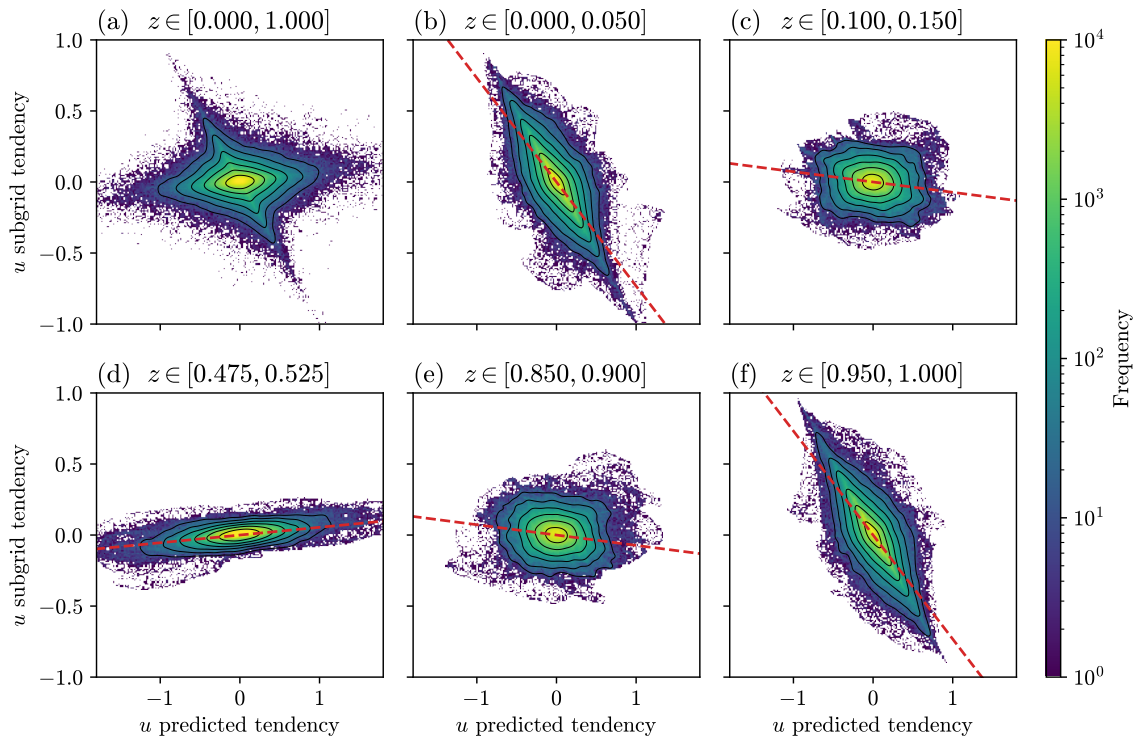


Figure 4.9: The equivalent of Figure 4.4 for the  $u$  subgrid tendency against the  $u$  tendency predicted by the coarse model.

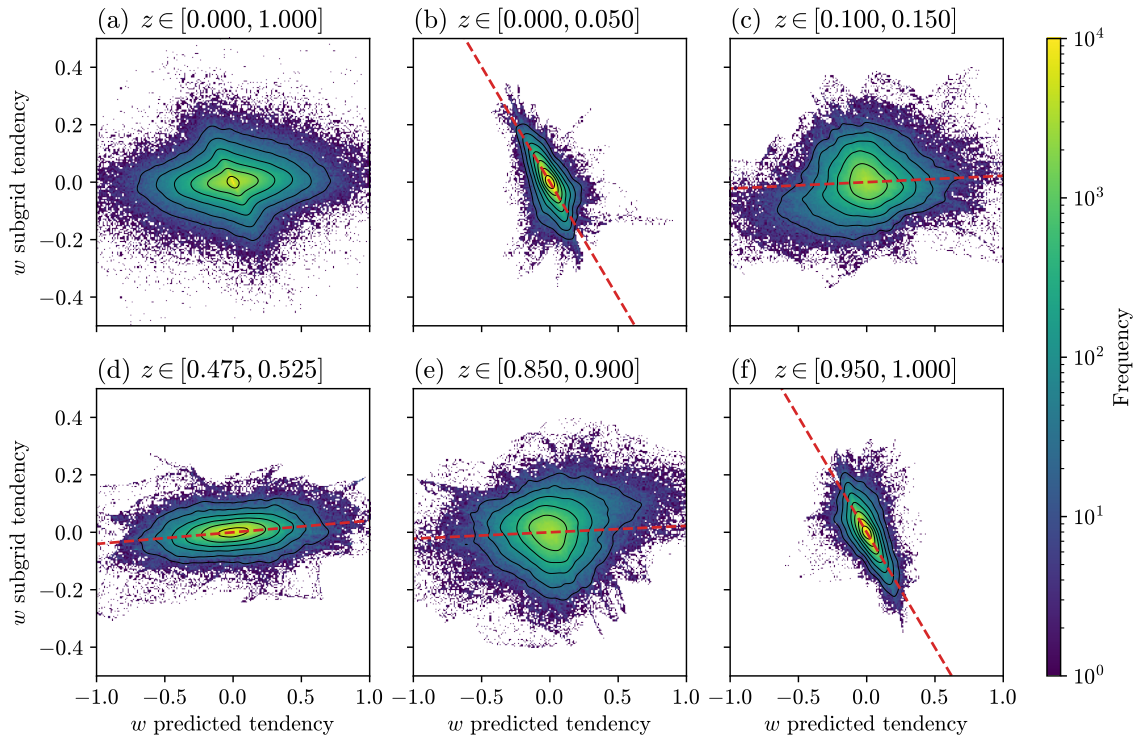


Figure 4.10: The equivalent of Figure 4.4 for the  $w$  subgrid tendency against the  $w$  tendency predicted by the coarse model.

*This page intentionally left blank*

# Bibliography

- Alieva, A., S. Hoyer, M. Brenner, G. Iaccarino, and P. Norgaard (2023). “Toward accelerated data-driven Rayleigh-Bénard convection simulations”. *Eur. Phys. J. E* **46**(7). DOI: [10.1140/epje/s10189-023-00302-w](https://doi.org/10.1140/epje/s10189-023-00302-w).
- Brajard, J., A. Carrassi, M. Bocquet, and L. Bertino (2021). “Combining data assimilation and machine learning to infer unresolved scale parametrization”. *Phil. Trans. R. Soc. A* **379**(2194). DOI: [10.1098/rsta.2020.0086](https://doi.org/10.1098/rsta.2020.0086).
- Jones, P. W. (1999). “First- and second-order conservative remapping schemes for grids in spherical coordinates”. *Mon. Weather Rev.* **127**(9). DOI: [10.1175/1520-0493\(1999\)127<2204:FASOCR>2.0.CO;2](https://doi.org/10.1175/1520-0493(1999)127<2204:FASOCR>2.0.CO;2).
- Stevens, R. J. A. M., R. Verzicco, and D. Lohse (2010). “Radial boundary layer structure and Nusselt number in Rayleigh-Bénard convection”. *J. Fluid Mech.* **643**. DOI: [10.1017/S0022112009992461](https://doi.org/10.1017/S0022112009992461).